

The High-fidelity Asteroid Deflection Evaluation Software (HADES): Assessing the Impact of Environmental and System Uncertainties on Autonomous Proximity Operations

By Massimo Vetrisano, Juan L. Cano and Simone Centuori

¹⁾ *Deimos Space S.L.U., Ronda de Poniente, 19, 28760 Tres Cantos, Madrid, Spain, +34 918063450, {massimo.vetrisano, juan-luis.cano, simone.centuori}@deimos-space.com*

(Received June 21st, 2017)

The High-fidelity Asteroid Deflection Evaluation Software (HADES) deals with the high-fidelity modelling of spacecraft operations at irregular shape asteroids. The software can handle any operational orbit, with particular care paid to fixed hovering configurations. Different control techniques based on both continuous and discrete methods have been considered and implemented. The manoeuvre execution itself can be affected by errors in magnitude and direction.

The spacecraft orbit determination can be performed either through a performance model or by on-board measurements, a navigation camera and a LIDAR, which are processed by an Unscented H-infinity Filter (UHF). HADES can employ different levels of accuracy between the assumed environment knowledge and the real world. The aim of this paper is to discuss in details the models that can be used to describe the dynamics and the estimation of a spacecraft hovering at an irregular object. It will show how the various modelling assumptions can affect the results regarding the control budget and on-board estimation in the highly perturbed environment of the comet 67P/Churyumov–Gerasimenko.

Key Words: GNC, Inertial Hovering, Non-uniform Gravity field, Optimal Control

Nomenclature

\mathbf{r}	: position vector
μ	: gravitational constant
SRP	: solar radiation pressure
\mathbf{u}	: control vector
A	: spacecraft cross section
m_{sc}	: spacecraft mass
S_{srp}	: solar radiation pressure at 1 AU
r_{1AU}	: astronomical unit in km
θ	: angular velocity of the asteroid orbit
U	: non-uniform gravity potential
$\mathbf{R}(\theta, \varphi)$: rotation matrix around 2 axis
\mathbf{P}	: covariance matrix
\mathbf{n}	: measurements noise
\mathbf{R}	: measurement noise covariance
\mathbf{G}	: controller gain
b	: control box
\bar{a}_p	: mean value of acceleration
\mathbf{Q}	: LQR controller gain on state error
\mathbf{U}	: LQR controller gain on the control
β	: linearized central body acceleration
\mathbf{A}	: constant discrete state matrix
\mathbf{B}	: constant discrete control matrix
\mathbf{S}	: matrix solution of Riccati equations
Δt	: time interval
$\Delta \mathbf{v}$: delta velocity
m	: manoeuvre execution error

\mathbf{z}	: measurements
\mathbf{K}	: Kalman gain
α	: performance bound in H_∞ filter
ξ	: scaling parameter
c	: ellipsoid semi-axes

Subscripts

a	: asteroid
sc	: spacecraft
0	: reference
k	: step
x	: state
z	: measurements
xz	: cross correlation state-measurments
nom	: nominal
est	: estimated
ref	: refernce

1. Introduction

In the last 20 years, there has been considerable progress in the exploration of the minor celestial objects by spacecraft. Recently the most remarkable mission has been Rosetta, which arrived at Comet 67P/Churyumov–Gerasimenko on 6 August 2014. The lander Philae achieved the first-ever soft landing on the surface of the comet on 12 November 2014. As shown by the difficulties on the identification of the final landing spot of the probe, the environment near minor bodies is pretty complex because of the lack of precise data where simplification regarding the shape and composition of the asteroid can drive to a completely incorrect picture of the

dynamics.

The navigation in close proximity of asteroids can be complicated due to the fact that the environment is uncertain, especially if the asteroid presents an irregular shape and rotation state. The motion of the spacecraft around the asteroid is, thus, highly nonlinear. Generally, the gravitational harmonics of the celestial minor bodies are estimated from on-board data collected during a close fly-by,¹⁾ during approach phases or by ground-based radar imaging data.^{2) 3)} Thus, it is necessary to evaluate possible different navigation strategies to increase the mission reliability and the possibility to cope with both unknown environment and system performance uncertainties.

One important aspect when designing proximity operations is to evaluate how the different control techniques and on-board instruments affect the performance of the system. The manoeuvre execution itself can be affected by errors in magnitude and direction.

This kind of missions typically requires the spacecraft to fly in a tight formation relatively close to the asteroid, so on-board estimation capabilities are desirable and indeed required when the delay time between ground and the spacecraft is too high to ensure the safety of operations.

Methods based on optical navigation camera and laser light radar (LIDAR) or laser range finder (LRF) integrated measurements have been proved to be a feasible option for a single spacecraft to approach or land on an asteroid.⁴⁾⁵⁾ Landmarks can also be considered when a map of the surface is available before the beginning of operations. The idea beneath this paper is to describe the operating environment a spacecraft will face at the asteroid, to show how the different assumption can affect the outcomes of the simulation. This can advise the reader on how to handle with the results and margins when it comes to the control budget for instance.

HADES is a high-fidelity simulation tool to assess GNC close proximity operations. Detailed models about the close proximity environment about Near Earth asteroids (NEA) and the involved operations are required during preliminary assessment of mission requirements especially under the presence of uncertainties. The implemented spacecraft dynamics considers the most relevant perturbations, i.e. third body effect from the Sun, solar radiation pressure (SRP) and irregular gravity field of the rotating asteroid. The software uses both spherical harmonics and actual asteroid's shape. In the first case the coefficients can be given from actual data or they are calculated on a user-defined ellipsoid; in the second case the gravity field is reconstructed from the asteroid tetrahedral mesh. The software can handle any operational orbit, with particular care paid to inertial and body fixed hovering. Different control techniques based on both continuous and discrete methods have been considered and implemented. HADES has a detailed model of camera and LIDAR, where the actual illumination and visibility conditions are modelled using real asteroid shape data. At initial stage one can also assume a performance model, but we will see how this can produce misleading results in reality.

We want to underline that we devoted detailed explanations

of the models in order for the interested readers to use them and recreate the results of the simulations, rather than retrieving all the information from diverse sources.

Thus this paper is organised as follows. Section 2 explains the different dynamic models and main modeling assumptions. In Section 3, the control technique used to maintain the spacecraft on its reference trajectory is briefly explained. Section 4 shows the estimation process through the Unscented H-Infinity filter and the assumed measurement models. Finally, Section 5 shows some obtained results. In particular, all the analyses for the GNC case are applied to the scenario of comet 67P/Churyumov–Gerasimenko whose shape model is well known after the visit of the mission Rosetta in 2015. The shape of the comet magnifies the possible source of mis-modelling which can affect the overall navigation. We considered inertial hovering configuration where the spacecraft maintains its location fixed with respect to the object. In particular we place the probe at 2.7 km, which is the periapsis distance of Rosetta's orbit.

2. Dynamic Models

In this section we want to give an accurate description of the models used to describe the dynamics of the spacecraft.

2.1. Hill's Reference Frame

In this section, we introduce the motion dynamics of spacecraft and asteroid in the non-inertial Hill's reference Frame (see Fig. 1). It is assumed that the asteroid body frame (later described) is coincident with this frame at the beginning of the simulations.

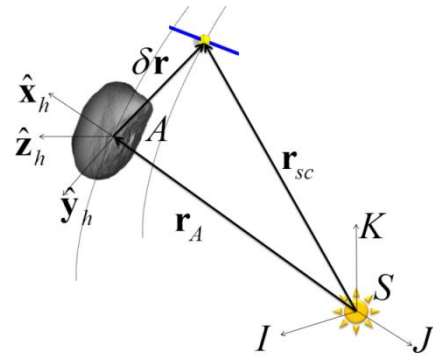


Fig. 1. Hill Reference Frames.

The spacecraft is subjected to the force due to solar gravity, solar radiation pressure and the asteroid's irregular gravity. The nonlinear relative equations of motion are given by:⁶⁾

$$\ddot{\mathbf{r}} + 2\dot{\boldsymbol{\theta}} \times \dot{\mathbf{r}} + \dot{\boldsymbol{\theta}} \times (\boldsymbol{\theta} \times \mathbf{r}) = -\mu_a/r^3 \mathbf{r} + \mu_{\text{Sun}} (\mathbf{r}_a / (r_a^3) - \mathbf{r}_{sc} / (r_{sc}^3)) + \partial U / \partial (\delta \mathbf{r}) + \mathbf{SRP}(\mathbf{r}_{sc}) + \mathbf{u} \quad (1)$$

$\dot{\boldsymbol{\theta}}$ represents the instantaneous angular velocity with which the asteroid (i.e. the reference frame) rotates around the Sun. $\mathbf{SRP}(\mathbf{r}_{sc})$ is the solar radiation pressure; $\mathbf{u} = [\mathbf{u}_x, \mathbf{u}_y, \mathbf{u}_z]$ is a control input for continuous control. In the case of impulsive control this term is null and impulsive variation of velocity is applied at the time of the manoeuvre.

U is the higher order potential of the asteroid.

The SRP depends on the distance from the Sun as the spacecraft exposed area, the reflectivity coefficient and the mass:

$$SRP(r_{sc}) = C_r S_{srp} \left(\frac{r_{1AU}}{r_{sc}} \right)^2 \frac{r_{sc}}{r_{sc}} \frac{A}{m_{sc}} \quad (2)$$

2.2. Asteroid motion around the Sun

The motion of the asteroid with respect to the Sun is given as:

$$\ddot{\mathbf{r}}_a = -\mu_{Sun}/(r_a^3) \mathbf{r}_a \quad (3)$$

Note that no perturbations acting on the asteroid are considered (i.e. Keplerian motion is assumed).

2.5. Gravity field models

The asphericity of these bodies gives raise to perturbations that affect all orbital elements, especially at low altitude. The models that have been considered to describe these effects are based on the standard Legendre polynomials of the gravity field potential as defined by Cunningham,⁷⁾ and on shape model.⁹⁾ The model works nicely when outside the object circumscribing sphere while it is completely unreliable inside. The use of Legendre polynomials allows an efficient computation of the potential and resulting perturbation as a function of the Cartesian coordinates in the body fixed reference frame. In the case of an ellipsoidal shape an analytical formula for calculating the even terms of the matrix \mathbf{C} is available.⁸⁾ The gravity model works for an arbitrary shape and was implemented from the equations used in⁹⁾. This model assumes a uniform asteroid density and allows expressing the local acceleration in an arbitrary location in space with respect to the asteroid's centre of mass. It is especially suited for proximity operations, where the harmonic techniques fail to provide an accurate representation of the gravity field.

3. Controller

We want to calculate the optimal gain matrix \mathbf{K} such that the state-feedback law $\mathbf{u}_k = -\mathbf{K}\delta\mathbf{x}_k$ (where k is the discrete step) minimizes the quadratic cost function

$$J(\mathbf{u}) = \sum_{k=1}^{\infty} \mathbf{x}_k^T \mathbf{Q} \mathbf{x}_k + \mathbf{u}_k^T \mathbf{U} \mathbf{u}_k$$

for the discretized state-space model of Eq. (6). Also in this case we neglected the contribution of the Coriolis force. For convenience we report the results:

$$\delta\dot{\mathbf{x}} = \begin{bmatrix} \mathbf{0}_{3 \times 3} & \mathbf{I}_{3 \times 3} \\ -\frac{\mu_a}{\delta r_0^3} [\mathbf{I} - 3\hat{\mathbf{r}}_0 \hat{\mathbf{r}}_0^T] & \mathbf{0}_{3 \times 3} \end{bmatrix} \delta\mathbf{x} + \begin{bmatrix} \mathbf{0}_{3 \times 3} \\ \mathbf{I}_{3 \times 3} \end{bmatrix} \mathbf{u} = \begin{bmatrix} \mathbf{0}_{3 \times 3} & \mathbf{I}_{3 \times 3} \\ \boldsymbol{\beta} & \mathbf{0}_{3 \times 3} \end{bmatrix} \delta\mathbf{x} + \begin{bmatrix} \mathbf{0}_{3 \times 3} \\ \mathbf{I}_{3 \times 3} \end{bmatrix} \mathbf{u} \quad (4)$$

$\boldsymbol{\beta} = \text{diag}([\beta_1, \beta_2, \beta_3])$. Integrating the equations of motion for a time step Δt using explicit Euler, one obtains

$$\delta\mathbf{x}_{k+1} = \begin{bmatrix} \mathbf{I} + \boldsymbol{\beta} \frac{\Delta t^2}{2} & \Delta t \mathbf{I}_{3 \times 3} \\ \boldsymbol{\beta} \Delta t & \mathbf{I}_{3 \times 3} \end{bmatrix} \delta\mathbf{x}_k + \begin{bmatrix} \Delta t \mathbf{I}_{3 \times 3} \\ \mathbf{I}_{3 \times 3} \end{bmatrix} \mathbf{u}_k = \mathbf{A}_k \delta\mathbf{x}_k + \mathbf{B}_k \mathbf{u}_k \quad (5)$$

\mathbf{A}_k and \mathbf{B}_k are constant discrete state matrix in this case. Then the state-feedback gain \mathbf{K} results:

$$\mathbf{K} = (\mathbf{B}_k^T \mathbf{S} \mathbf{B}_k + \mathbf{R})^{-1} \mathbf{B}_k^T \mathbf{S} \quad (6)$$

\mathbf{S} is given by the solution of the discrete-time Riccati equation:

$$\mathbf{A}_k^T \mathbf{S}^T \mathbf{A}_k - \mathbf{S} - \mathbf{A}_k^T \mathbf{S} \mathbf{A}_k (\mathbf{B}_k^T \mathbf{S} \mathbf{B}_k)^{-1} \mathbf{B}_k^T \mathbf{S} \mathbf{A}_k + \mathbf{Q} = \mathbf{0} \quad (7)$$

Although the controller will work using only proportional correction manoeuvre, we decided to add the integrative contribution due to the action of the gravity field during the interval between corrections. The integrative contribution improves the accuracy because otherwise the spacecraft will tend to move towards an artificial equilibrium point where

$$\frac{c_p}{c_d} = -\frac{\delta v_{est} - \delta v_{ref}}{\delta r_{est} - \delta r_{ref}} \quad (8)$$

We assume that the overall effect from the other forces is negligible and the LQR is able to cope with those perturbations. The integrative contribution is calculated assuming a constant acceleration:

$$\mathbf{u}_k = \mathbf{G} \delta\mathbf{x}_k - \bar{a}_p \Delta t \hat{\mathbf{r}}_0 \quad (9)$$

\bar{a}_p is the mean value of acceleration as measured at centre, superior and inferior edge of the control box defined by a characteristic length, b , used to calculate the gain. The integrative contribution was added only when contribution of the perturbations does not work to reduce the position error. This is done simply to include the fact that the gravity acts favourably by attracting the spacecraft towards the reference position when the spacecraft is above the nominal altitude. We required the controller to perform the maximum delta- v manoeuvre equal to $2v_{acc}$ when the error in position (on components base) is equal to b and the velocity error is v_{acc}

(where v_{acc} is the velocity acquired by constant gravitational acceleration during a free fall along b). This means that:

$$\mathbf{Q} = \text{diag}([b \ b \ b \ v_{acc} \ v_{acc} \ v_{acc}]^{-2})$$

$$\mathbf{U} = \text{diag}([2v_{acc} \ 2v_{acc} \ 2v_{acc}]^{-2}) \quad (10)$$

In practice, if the spacecraft started moving from the nominal stated, a reflection manoeuvre would be performed at the edge of the control box. Error in the manoeuvre execution has been modelled in terms of magnitude and direction as:

$$\Delta \mathbf{v} = \mathbf{R}(\theta, \varphi) \Delta \mathbf{v}_{nom} (1 + m) \quad (11)$$

where $\Delta \mathbf{v}_{nom}$ is the nominal manoeuvre, and θ, φ are the error angles on two directions. The errors are generated randomly consistently with the assumed execution error statistics.

4. Navigation Models

The Navigation Module conceptually contains two trajectory estimation routines

1. A performance model based on typical knowledge of the spacecraft trajectory.
2. A real-time on board filter based on the Unscented H-infinity Filter (UHF) which uses LIDAR and camera measurements.

The first is a simple performance model for the orbit determination which consists of pseudo state vector measurements \mathbf{z} simply given as.

$$\mathbf{z} = [\mathbf{r} \ \mathbf{v}] + \mathbf{n} \quad (12)$$

Note that the measurement error is given along track and across track, thus a transformation from the local rotating frame to the Cartesian one is performed. In the second case the estimate is calculated as the filter state vector $\tilde{\mathbf{x}}_k$, and covariance updated matrix \mathbf{P}_k are represented as follows

$$\tilde{\mathbf{x}}_k = \tilde{\mathbf{x}}_k^- + \mathbf{K}(\mathbf{y}_k - \hat{\mathbf{y}}_k^-)$$

$$(\mathbf{P}_k)^{-1} = (\mathbf{P}_k^-) + (\mathbf{P}_k^-)^{-1} \mathbf{P}_{xz,k} \mathbf{R}_k^{-1} [(\mathbf{P}_k^-)^{-1} \mathbf{P}_{xz,k}]^T - \alpha_k \mathbf{I}_d \quad (13)$$

$$\mathbf{K} = \mathbf{P}_{xz,k} \mathbf{P}_{z,k}^{-1}$$

The predicted mean of the state vector $\tilde{\mathbf{x}}_k^-$, the covariance matrix \mathbf{P}_k^- and the mean observation $\hat{\mathbf{y}}_k^-$ can be approximated using the weighted mean and covariance of the transformed set of sigma points.^{10,11)} \mathbf{R}_k is a suitable matrix which in the case of normal distribution coincides with the measurement noise covariance matrix at time step k . In order to assure that the covariance matrix is positive definite, this value is calculated at each iteration as:¹¹⁾

$$\alpha_k^{-1} = \xi_{\max} \left(\text{eig} \left((\mathbf{P}_k^-)^{-1} (\mathbf{P}_k^-)^{-1} \mathbf{P}_{xz,k} \mathbf{R}_k^{-1} [(\mathbf{P}_k^-)^{-1} \mathbf{P}_{xz,k}]^T \right)^{-1} \right) \quad (14)$$

The hypothesis underneath the generic Kalman filter is that the noise in measurements, dynamic model and priors is Gaussian in nature. This might not be the case in general and even though the UKF has proven to work reasonably well when the Kalman filter hypotheses are not satisfied, a better alternative would be to use a H_∞ filter, also called minmax filter. The H_∞ filter does not require prior assumptions on the nature of the noise, and minimizes the worst-case estimation error. The choice of the H_∞ filter is preferable when the Gaussian hypothesis cannot be fully guaranteed, for example when biases in the instruments are not detected.^{10,11)} In our case, besides biases affecting all the instruments, the LIDAR measurements are affected by the camera process and errors. Therefore, the noise introduced by the LIDAR cannot be modelled as an uncorrelated white noise. In order to deal with nonlinearities, one can use an extension to the H_∞ filter, the Extended H_∞ Filter (EHF), analogous to the extended Kalman filter. In this case, however, some hypotheses need to be introduced on the smoothness and regularity of the process and measurements. An alternative is to introduce the unscented transformation in the H_∞ filter to avoid the approximation of the Jacobian matrices,¹¹⁾ and build an Unscented H_∞ Filter.

4.1. Instruments Model

Two instruments are considered for performing navigation: a navigation camera and a LIDAR. It is assumed that the attitude of the spacecraft is known with a level of precision corresponding to the one of the star tracker on two axes. We assumed two kind of image processing:

1. The camera identifies the centroid on the body surface based on the actual illumination conditions.
2. The camera identifies land-marks points on the surface.

The measurement from the camera is affected by the spacecraft attitude pointing, the pixelization and the centroiding errors (where the last one is the mismatch between centroid and centre of mass). The pixelization error is due to the fact that the image of the asteroid is formed by a discrete number of pixels. This is sensible if one assumes that a complementary map could be built while starting the orbit acquisition, combining the pictures. For what concerns the LIDAR, it generally provides range from the spacecraft to a point on the surface of target object and works at a range from 50 m to 50 km. It is assumed that the LIDAR illuminates the point on the surface that corresponds to the centroid derived from the elaboration of the images acquired by the camera.¹³⁾ The actual illumination and visibility condition are considered such that the image on the screen of the camera will be as shown in an example of Fig. 2, where the centre of brightness

has been represented along with the footprint of the LIDAR on the surface as taken around it. In the bottom, it shows the som landmarks on the area visible to a 12 degrees FoV camera.

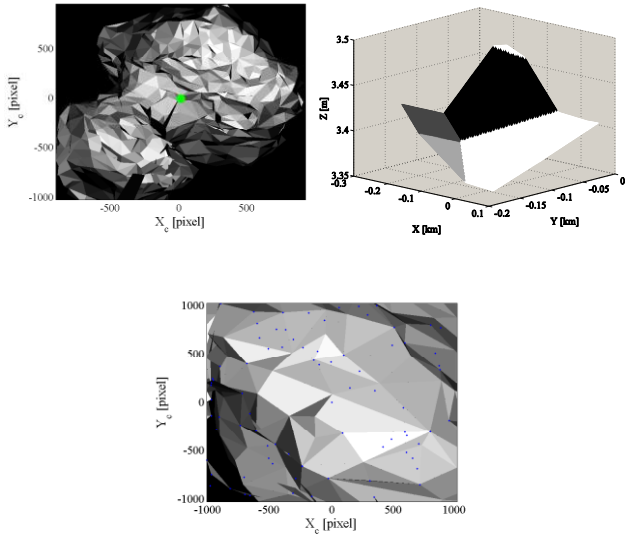


Fig. 2. Example of image as seen on the screen of the camera generated using the Comet 67P/Churyumov–Gerasimenko (left), footprint of the LIDAR around the corresponding centre of brightness (right), landmarks points (blue dots bottom).

5. Case Study

In the following, we will move from simpler to more complex models, showing how the different assumptions can lead to dissimilar results, especially for what concerns the control budget. We considered a number of four different cases:

1. The comet shape is assumed to be an ellipsoid, thus gravity field is described as an 8th order ellipsoidal field and a performance model is used for the estimated trajectory.
2. The gravity field of the comet is given by the actual spherical harmonics, and a performance model is employed for navigation purposes.
3. Same as above, but the estimated trajectory is obtained through filtering where the gravity order is reduced with respect to the real one, and the shape of the comet is an ellipsoid whose mean radius for the measurements model differs by 1% error from the actual radius.
4. In this case the dynamics and the measurements are given by the actual shape of body, while the filter relies on the harmonics, and the mean radius for its measurement model differs by 1% error from the actual one. The gravity field in the real world is generated using the actual shape, while the filter relies only on a third order gravity field.

In the following, we first introduce the environment in Section 5.1 and the spacecraft operative conditions in Section

5.2. We then analysis the characteristic trend for the single simulation in Section 5.3 and eventually we discuss the results with the aid of a Monte Carlo simulation to draw some statistical conclusions in Section 5.3.5.

5.1. Comet Comet 67P/Churyumov–Gerasimenko

In the followings, the analysed methods are tested. Besides the calculation of mere control figures as the navigation budget, the comparison is based also on the capability to control the spacecraft with a limited number of actuations. The minor body selected was the Comet 67P/Churyumov–Gerasimenko, whose Keplerian elements are reported in see Table 1. The motion of the asteroid around the Sun was considered purely Keplerian without any perturbation and simulations start from perigee. Moreover there is no effect of the coma included in the simulation. The asteroid was assumed to be shaped as an ellipsoid of semi-axes $[c_1 \ c_2 \ c_3] = [2.530 \ 1.857 \ 1.656]$ km. For reference to the next analyses, where the shape of the comet will be used in the dynamics as well as in the measurements generation, Fig. 3 shows the 3D mesh of the well-known duck-shape comet.

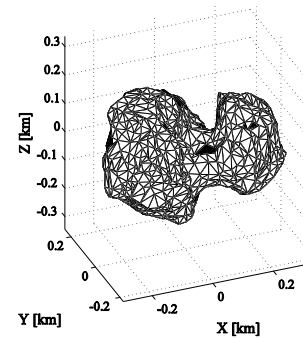


Fig. 3. Shape of Comet 67P/Churyumov–Gerasimenko.

Assuming such a shape allows calculating the gravitational harmonics analytically.⁸⁾ When we will consider the actual shape, we used the denormalized Stokes coefficients for the third order degree,⁸⁾ as reported in Table 1. The gravity constant from the asteroid is thus $6.67259 \cdot 10^{-7}$ km/s³.

Table 1. Comet 67P/Churyumov–Gerasimenko from JPL database.

Items	Values
a [AU]	3.464805313920435
e	.6414365761974745
i [deg]	7.04529818125678
ω [deg]	50.08466699140272
Ω [deg]	12.84210194638212
C_{20}	-7.93×10^{-2}
C_{22}	2.71×10^{-2}
C_{30}	-1.36×10^{-2}
C_{31}	10^{-2}
$C_{32}, C_{33}, S_{31}, S_{32}, S_{33}$	10^{-3}
C_{22}	10^{-4}
C_{11}, S_{21}	10^{-13}
$C_{10}, S_{11}, S_{21}, S_{22}$	10^{-14}

The asteroid rotates around c_3 axis every 12.4043 hrs with the equatorial plane coincident with the asteroid orbital plane at the beginning of the simulation (c_1 and c_2 aligned with x-y of the Hill reference frame).

5.2. Spacecraft characteristics

The initial nominal condition of the spacecraft was randomly generated around the nominal operational trajectory in the local Hill's frame (radial, tangential and out of plane components – position in km, velocity in km/s):

$$\begin{bmatrix} x & y & z & v_x & v_y & v_z \end{bmatrix} = [-5.2 \text{ km } 0 \ 0 \ 0 \ 0 \ 0]$$

We arbitrarily decided to place the spacecraft at about 2.7 km from the surface of the comet (considering the maximum semi-axis c_1) as it was the periapsis distance of Rosetta. Table 2 reports the characteristics of the sensors assembly.

Table 2. Measurements assembly characteristics	
Items	Values
Lidar mounting error	0.001 deg
Lidar range error	20 m
Lidar range bias	1 m
Number of pixels per side	2048
Camera FoV	40 deg
WAC FoV	12 deg
NAV FoV	2.4 deg
Attitude error	0.0057 deg
Attitude bias	0.0006 deg

We first assumed a 40 degree wide angle camera; otherwise the asteroid would not be contained in the camera screen, and then we employ a WAC and a NAC which were on-board of the mission Rosetta to simulate the land-marks scenarios. The spacecraft is assumed to have an area to mass ratio of $0.0393 \text{ m}^2/\text{kg}$ and an equivalent reflectivity coefficient (given by reflection and diffusion) of 1.3. We considered an actuation error of 3% (3σ) on magnitude and 2 degrees on angles (3σ). For the navigation we used the performance model where the pseudo state vector was known with 20 m along track, 10 m cross track in position and 2 mm/s along track and 1 mm/s cross track in velocity (all the quantities are 1σ). We used an error of 20 m just to have an along track error comparable to the one obtained using extensive radiometric measurements.

For what concerns the controller, the gain b was set to 30 m and manoeuvres below 1 cm/s were not executed. The actuation time was coincident with the measurements frequency of 10 minutes.

5.3. Results

In this section, we want to see how different dynamics and measurements model affect the performance of the state estimate along with the navigation budget. In the following we will show the trend for the controlled and estimated trajectory when a filter is employed. In any case the random number generator was set to the same value at the beginning of simulation in order to present consistent results. The spacecraft is placed on the nominal trajectory, while in

Section 5.3.5 we will report the statistical control budget obtained by modifying the initial conditions, accordingly with the initial filtering guess of 50 m on position and 2 cm/s in velocity for each component.

5.3.1. Case 1- Ellipsoid shape and performance model

The first analysed case can be considered a first guess, where the control performance can be preliminary tested, under a typical trajectory knowledge from ground station. The fact comet shape is assumed to be an ellipsoid and the gravity field is described as an 8th order ellipsoidal field simplifies considerably the dynamics. Fig. 4 shows the trend for the controlled position and velocity. As one can see, the trajectory error is confined between 30 m boundaries and the maximum velocity error is in the range of 2 cm/s, basically due to a combination of control capabilities and actuation error. The peak along y direction is due to the rotation of the comet with subsequent strong variation of the gravity field after 12 hours when the distance of the spacecraft with respect to the surface is the minimum.

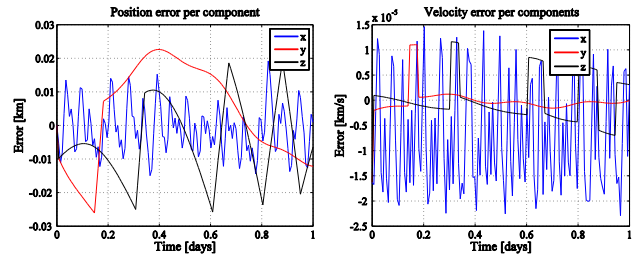


Fig. 4. Case 1: controlled position (left) and velocity (right).

5.3.2. Case 2- Spherical harmonics and performance model

Although the spacecraft motion results confined as in Case 1, the variation of the gravity field of due to the actual spherical harmonics is stronger driving the spacecraft outside the 30 m boundaries, see Fig. 5.

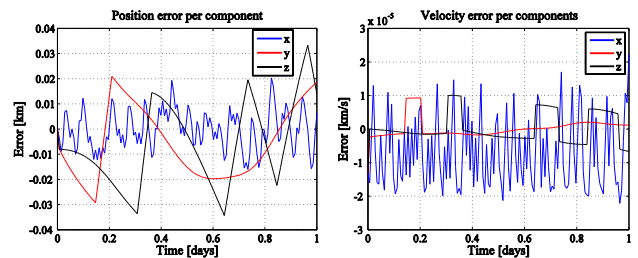


Fig. 5. Case 2: controlled position (left) and velocity (right).

This case also shows the limitation of using the linearized approach of Section 3 to calculate the controller gains. Time varying gains accordingly to the relative configuration of the spacecraft could improve the overall controller performance and could be analysed in future works.

5.3.3. Case 3- Spherical harmonics and filtering

In this case, we employ the on-board system to estimate the trajectory of the spacecraft. The gravity field in the filter is known to second degree harmonics, while shape of the comet

is assumed to be an ellipsoid whose mean radius for the measurements model differs by 1% error from the actual radius. Fig. 6 shows the controlled trajectory where one can see that the controlled position error is biased along the x direction where the combination of the gravity field and the lack of shape knowledge produce the maximum effect. In fact from Fig. 7, we see that the estimation error itself is biased along the x-axis by a value that in mean terms is about 25 m that is consistent with 1% size error. Note that the lack of harmonics leads the filter to place the spacecraft closer to the comet (negative sign along x error). In Fig. 6 right, we see that as a consequence of the estimation error also the controlled velocity error is in general increased with respect to Case 2. If we compare its trend with the one of Fig. 5 we see that the difference is mainly due to the estimated velocity (Fig. 7 right).

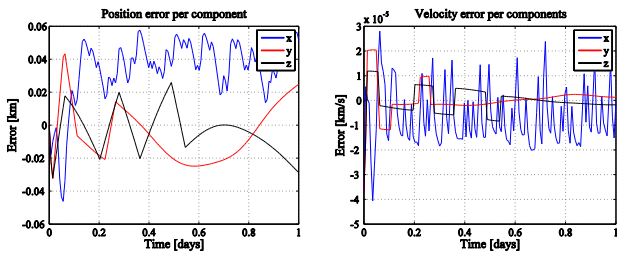


Fig. 6. Case 3: controlled position (left) and velocity (right).

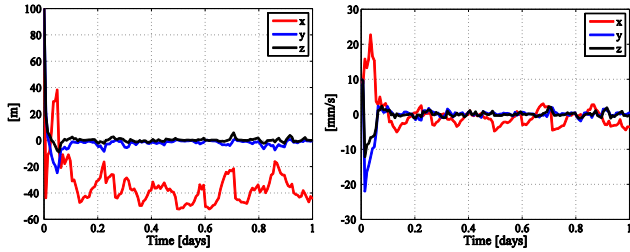


Fig. 7. Case 3: estimated position (left) and velocity (right).

5.3.4. Case 4- Shape model and filtering

In this case the dynamics and the measurements are given by the actual shape of body, while the filter relies the third order gravity field of Table 1, and the mean radius for its measurement model differs by 1% error from the actual one. This case is the most interesting because it allows us to

1. demonstrate the effect of the size of the asteroid in terms of accuracy of the mesh; for computational convenience we use a baseline coarse mesh in the filter of 100 facets and we compare the results with respect to a 1000 facets shape;
2. evaluate the impact of the on-board processing on the performance; spacecraft computer have limited computational capabilities, so fixed-time step integrator are used to reduce the computation burden; a fixed step Runge-Kutta of order five for all the time-integrations is employed in the filter;

3. analyse the use of wide and narrow angle cameras to identify landmarks on the visible spots with the on-board processing.

Fig. 8 and Fig. 9 show the controlled and estimated trajectory trends in the case the shape model used for both the real world camera and the filter is a 1000 facets polyhedron. On the contrary of Case 3, the filter positions the spacecraft farther from surface (Fig. 9 left) and the error is in the range of 25, which is 1% of the major semi-axis. This produces also a velocity error which biased along x. The higher control errors are as a consequence along x (see Fig. 8). Nonetheless the overall system manages to contain the spacecraft within 50 m error from the reference position.

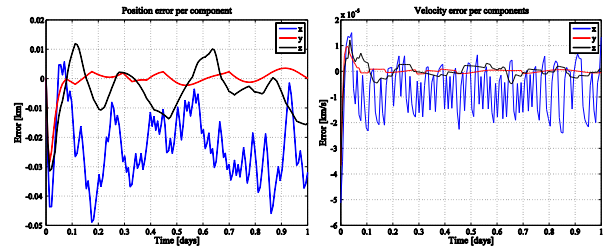


Fig. 8. Case 4 using a 1000 faces mesh for the asteroid surface: controlled position (left) and velocity (right).

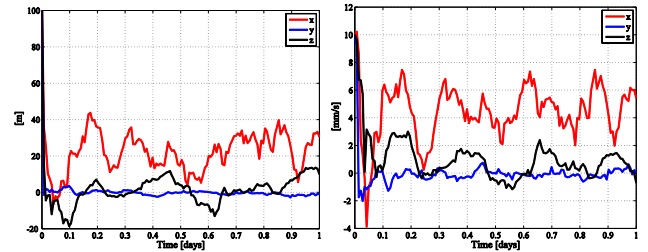


Fig. 9. Case 4 using a 1000 faces mesh for the asteroid surface: estimated position (left) and velocity (right).

Fig. 10 and Fig. 11 show that similar trend are obtained when the on-board system relies on simplified surface models with 100 facets polyhedron.

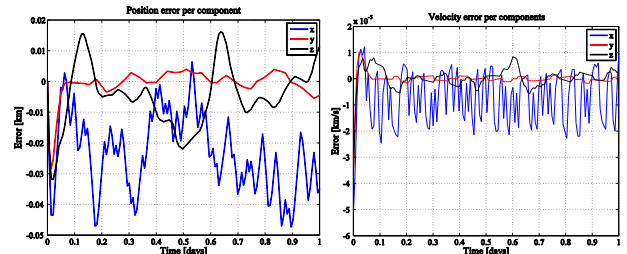


Fig. 10. Case 4 using a 100 faces mesh for the asteroid surface: controlled position (left) and velocity (right).

The main difference can be seen on the controlled and estimated trajectory peaks which are slightly higher than the ones in the 1000 facets case.

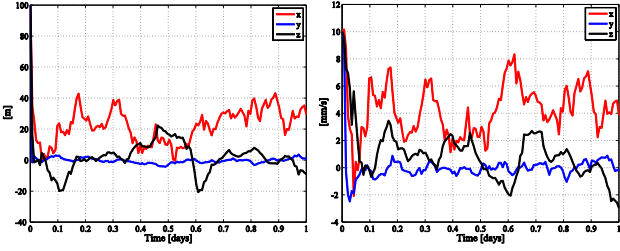


Fig. 11. Case 4 using a 100 faces mesh for the asteroid surface: estimated position (left) and velocity (right).

Eventually, if the computational capabilities are limited to a fixed-step time integrator, we obtain that the overall errors are further amplified. With reference to Fig. 12 and Fig. 13, we see that the controller and the filter errors are above the 50 m we have seen in the previous case. Also the velocity periodically exceeds 1 cm/s error.

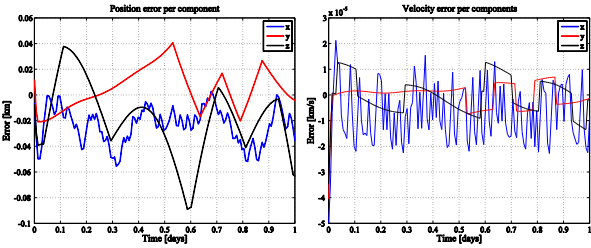


Fig. 12. Case 4 using a 100 faces mesh for the asteroid surface and on-board fixed step integrator: controlled position (left) and velocity (right).

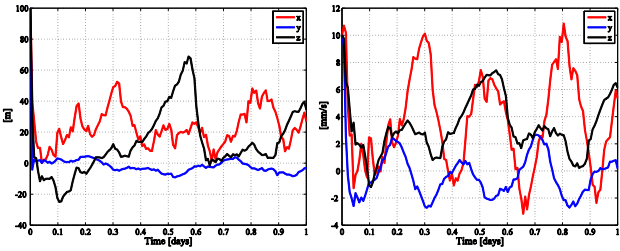


Fig. 13. Case 4 using a 100 faces mesh for the asteroid surface and on-board fixed step integrator: estimated position (left) and velocity (right).

This is due to the discrepancy between the measurement model in the filter and the actual model, as well to the strong sensitivity of the dynamics to the variation of the conditions and numerical errors which mislead the filter to wrong estimate.

The next set of figures (from Fig. 14 to Fig. 17) shows the results for controlled and estimated trajectory using a WAC and a NAC. The same conditions as in the previous case have been used. The most noticeable thing about the use of the landmarks is that the controlled and estimated trajectory result to be more accurate with respect to the analysed examples of this section. Using the NAC, the overall control-navigation system is able to maintain the spacecraft within the assumed boundaries. In any case, the expected error would be in the range of the difference between the on-board model and the

real world, unless the navigation system is not able to estimate a corrective factor to fit the measurements with its own on-board models.

Although from this single simulation is not clearly possible to deduce it, the fact that NAC can identify the points on the surface more accurately has beneficial effects on the navigation and the controlled trajectory. This trend will be more clearly shown with the MC simulations in the next section.

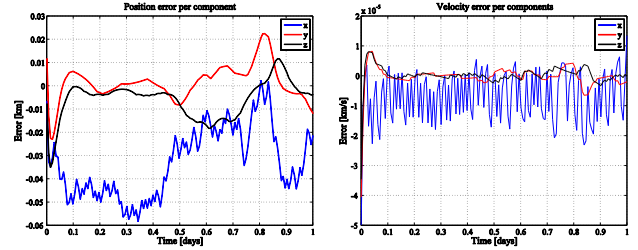


Fig. 14. Case 4 using a 100 faces mesh, on-board fixed step integrator, landmarks with WAC: controlled position (left) and velocity (right).

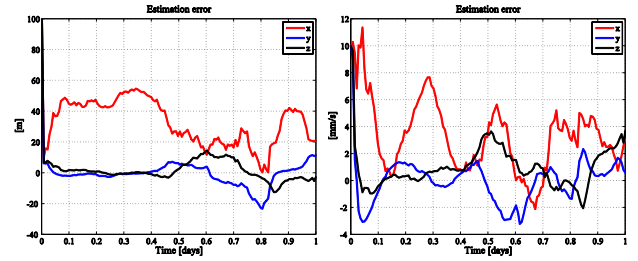


Fig. 15. Case 4 using a 100 faces mesh, on-board fixed step integrator, landmarks with WAC: estimated position (left) and velocity (right).

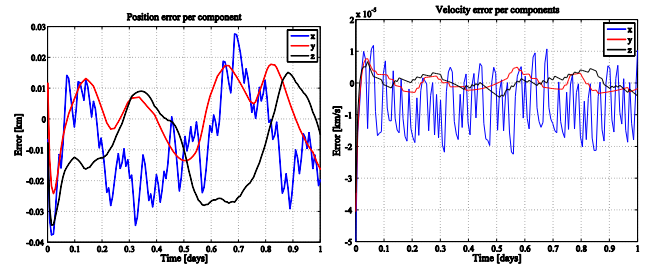


Fig. 16. Case 4 using a 100 faces mesh, on-board fixed step integrator, landmarks with NAC: controlled position (left) and velocity (right).

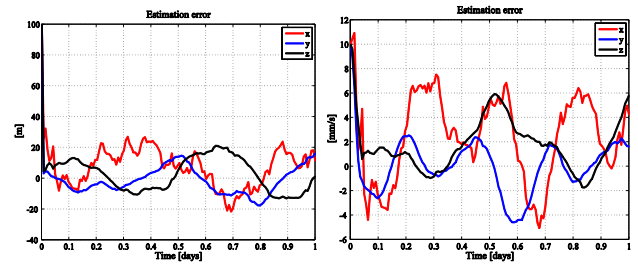


Fig. 17. Case 4 using a 100 faces mesh, on-board fixed step integrator, landmarks with NAC: estimated position (left) and velocity (right).

5.3.5. Summary

An important factor is represented by the impact of the environment as well as the system assumptions on the control budget. Of course the number of uncertain parameters which can affect this figure tends to diminish thanks to extensive

ground support prior the start of and during operations. Nonetheless good models can help mission designer and system engineers to use more refined values and predict which will be the behavior of the system. For the above cases, we performed a Monte Carlo analysis consisting in 200 independent realizations where the initial trajectory and initial filter guess was drawn from a normal distribution with a dispersion of 50 m and 2 cm/s in position and velocity, respectively. We did not consider the 1000 facets polyhedron case because the difference with respect to the 100 facets was marginal, as well for the high computational cost.

The effect on the Δv in terms of mean and standard deviation is reported in Table 3. We see that as we move from simpler models to more complex ones, the control budget tends to increase monotonically. Also the dispersion appears to increase, although Case 2 displays a slightly higher dispersion with respect to Case 3, which is caused by the fact that in this configuration the spacecraft is systematically place closer to the surface, thus the deviation are magnified. Among the most fidelity models, the use of a NAC is the one presenting the minimum mean value, with also the smallest dispersion thanks to the better precision of the navigation system.

Table 3. Impact of different modelling assumptions of the performance of the control budget.

Scenario	Mean Δv [m/s]	1-sigma Δv [m/s]
Case 1	2.1816	0.023907
Case 2	2.1922	0.024455
Case 3	2.2094	0.019932
Case 4	2.2431	0.019559
Case 4 OB	2.2748	0.025643
Case 5 OB+WAC	2.1200	0.023470
Case 6 OB+NAC	2.1156	0.01996

If we consider a level of confidence of 99.7 (corresponding to 3-sigma), we see that the maximum difference in control budget is about 16%, obtained considering minimum 3-sigma value for case 5 and the maximum 3-sigma budget for case 4.

6. Conclusions

This paper presented a comparative assessment on how the different modelling assumptions can affect the overall control and navigation performance. For this purpose we used the main features of the High-fidelity Asteroid Deflection Evaluation Software developed at Deimos Space S.L.U. for close proximity operations. In order to stress the effects from the uncertain environment we considered the duck-shaped 67P/Churyumov-Gerasimenko, whose gravity field cannot easily model. In this way we could assess how the knowledge of the environment affects the navigation and the control

budget. We showed and compare several cases and we focused on the navigation performance for different level of environment knowledge, assuming shape and harmonics models for the gravity field and the measurements generation.

In general if we use a performance model and the environments is quite predictable or well known the performance of the controller does not differ much from the one obtained with relatively more accurate models. When the environment is pretty unknown the difference could differ significantly, although where we place the spacecraft in principle affects the subsequent results. From the analysis, one can deduce that the navigation by landmarks outperforms the navigation system by ranging and centroid measurements as expected.

From the analysed cases we have seen that the control budget difference can be as high as 16%. Although this level is often absorbed by safety margin which can be 20% for known environment or as high as 100% for highly perturbed and uncertain minor objects, this work and HADES can be applied to several other analysis. For instance if the size of the asteroid is roughly known as well as its composition and rotational motion, we could perform extensive analysis based on different shapes, masses and angular velocities to draw accurate predictions of the control and navigation performance.

Acknowledgements

The presented work has been developed within the European Commission's Framework Programme 7 funded Stardust project, through the Stardust Marie Curie Initial Training Network, FP7-PEOPLE-2012-ITN, Grant Agreement 317185.

References

- 1) T. Morley, F. Budnik, "Rosetta Navigation for the fly-by of the asteroid 2867 Steins", Proceedings of the 21st International Symposium on Space Flight Dynamics. Toulouse, France, 2009.
- 2) D.J. Scheeres, R. Gaskell, S. Abe, O. Barnouin-Jha, T. Hashimoto, J. Kawaguchi, T. Kubota, J. Saito, M. Yoshikawa, N. Hirata, T. Mukaik, M. Ishiguro, T. Kominato, K. Shirakawa and M. Uo, "The Actual Dynamical Environment About Itokawa", AIAA/AAS Astrodynamics Specialist Conference and Exhibit, Keystone, Colorado, 21 - 24 August 2006.
- 3) D.J. Scheeres, S. Broschart, S.J. Ostro and L.A. Benner, "The Dynamical Environment About Asteroid 25143 Itokawa: Target of the Hayabusa Mission", AIAA/AAS Astrodynamics Specialist Conference and Exhibit. Providence, Rhode Island 16 - 19 August 2004.
- 4) T. Kubota, T. Hashimoto, S. Sawai, J. Kawaguchi, K. Ninomiya, M. Uoc, K. Babac, "An autonomous navigation and guidance system for MUSES-C asteroid landing", Acta Astronautica 52 (2003) 125 - 131.
- 5) S. Li, P. Cui and H. Cui, "Autonomous navigation and guidance for

- landing on asteroids*”, Aerospace science and technology, 10(3): 239-247, 2006
- 6) D. J., Scheeres, “*Orbital Motion in Strongly perturbed Environments. Applications to Asteroid, Comet and Planetary Orbiters. 1st editio*”n, Springer-Praxis books in astronautical engineering. 2011
 - 7) O., Montenbruck and E., Gill, “*Satellite Orbits: Models, Methods and Applications*”, Springer-Verlag, Heidelberg, 2005.
 - 8) W. Boyce, “*Comment on a formula for the gravitational harmonic coefficients of a triaxial ellipsoid*”, Celestial Mechanics and Dynamical Astronomy, Volume 67, Issue 2, pp 107-110, February 1997
 - 9) T. Winkler, B. Kaplinger and B. Wie, “*Optical Navigation and Fuel-Efficient Orbit Control around an Irregular-Shaped Asteroid*”, AIAA Guidance, Navigation, and Control (GNC) Conference, Boston, USA, 08/2013.
 - 10) D. Simons, “*Optimal state estimation, Kalman, and Non-linear Approaches*”, Published by John Wiley & Sons, Inc., Hoboken, New Jersey, 2006.
 - 11) W. Li, and Y. Jia, “*H-infinity filtering for a class of nonlinear discrete-time systems based on unscented transform*”, Signal Processing 90(2010)3301–3307, 2010.
 - 12) S.M Oh and E.N. Johnson, “*Relative Motion Estimation for Vision-based Formation Flight using Unscented Kalman Filter*”, AIAA Guidance, Navigation and Control Conference and Exhibit, Hilton Head, South Carolina, 2007.
 - 13) K. Dionne, “*Improving Autonomous Optical Navigation for Small Body Exploration Using Range Measurements*”, AIAA 2009-6106. AIAA Guidance, Navigation, and Control Conference, 10 - 13 August 2009, Chicago, Illinois.
 - 14) C. Lhotka, S. Reimond, J. Souchay and O. Baur, “*Gravity field and solar component of the precession rate and nutation coefficients of Comet 67P/Churyumov–Gerasimenko*”, in Monthly Notices of the Royal Astronomical Society, Volume 455, Issue 4, p. 3588-3596, December 2015.